

Article

# Design and Embedded Implementation of Secure Image Encryption Scheme Using DWT and 2D-LASM

Heping Wen <sup>1,2,\*</sup>, Zefeng Chen <sup>1</sup>, Jiehong Zheng <sup>1</sup>, Yiming Huang <sup>1</sup>, Shuwei Li <sup>1</sup>, Linchao Ma <sup>1</sup>, Yiting Lin <sup>1</sup>, Zhen Liu <sup>1</sup>, Rui Li <sup>1</sup>, Linhao Liu <sup>1</sup>, Wenxing Lin <sup>1</sup>, Jieyi Yang <sup>1</sup>, Chongfu Zhang <sup>2,\*</sup> and Huaide Yang <sup>3</sup>

<sup>1</sup> School of Electronic Information, Zhongshan Institute, University of Electronic Science and Technology of China, Zhongshan 528402, China

<sup>2</sup> School of Information and Communication Engineering, University of Electronic Science and Technology of China, Chengdu 611731, China

<sup>3</sup> School of Electronic Information, Dongguan Polytechnic, Dongguan 523808, China

\* Correspondence: wenheping@uestc.edu.cn (H.W.); cfzhang@uestc.edu.cn (C.Z.)

**Abstract:** In order to further improve the information effectiveness of digital image transmission, an image-encryption algorithm based on 2D-Logistic-adjusted-Sine map (2D-LASM) and Discrete Wavelet Transform (DWT) is proposed. First, a dynamic key with plaintext correlation is generated using Message-Digest Algorithm 5 (MD5), and 2D-LASM chaos is generated based on the key to obtain a chaotic pseudo-random sequence. Secondly, we perform DWT on the plaintext image to map the image from the time domain to the frequency domain and decompose the low-frequency (LF) coefficient and high-frequency (HF) coefficient. Then, the chaotic sequence is used to encrypt the LF coefficient with the structure of “confusion-permutation”. We perform the permutation operation on HF coefficient, and we reconstruct the image of the processed LF coefficient and HF coefficient to obtain the frequency-domain ciphertext image. Finally, the ciphertext is dynamically diffused using the chaotic sequence to obtain the final ciphertext. Theoretical analysis and simulation experiments show that the algorithm has a large key space and can effectively resist various attacks. Compared with the spatial-domain algorithms, this algorithm has great advantages in terms of computational complexity, security performance, and encryption efficiency. At the same time, it provides better concealment of the encrypted image while ensuring the encryption efficiency compared to existing frequency-domain methods. The successful implementation on the embedded device in the optical network environment verifies the experimental feasibility of this algorithm in the new network application.



**Citation:** Wen, H.; Chen, Z.; Zheng, J.; Huang, Y.; Li, S.; Ma, L.; Lin, Y.; Liu, Z.; Li, R.; Liu, L.; et al. Design and Embedded Implementation of Secure Image Encryption Scheme Using DWT and 2D-LASM. *Entropy* **2022**, *24*, 1332. <https://doi.org/10.3390/e24101332>

Academic Editor: Amelia Carolina Sparavigna

Received: 18 August 2022

Accepted: 19 September 2022

Published: 22 September 2022

**Publisher's Note:** MDPI stays neutral with regard to jurisdictional claims in published maps and institutional affiliations.



**Copyright:** © 2022 by the authors. Licensee MDPI, Basel, Switzerland. This article is an open access article distributed under the terms and conditions of the Creative Commons Attribution (CC BY) license (<https://creativecommons.org/licenses/by/4.0/>).

## 1. Introduction

With the rise of big data and the development of digital image processing technology [1–5], the digital image as an important transmission medium, contains a large amount of important data, such as personal privacy and confidential information. The importance of secure transmission is self-evident. However, in contrast to textual information, digital image information is characterised by high complexity and strong pixel correlation [6–8]; therefore, it is essential to study encryption algorithms for digital images.

In order to realize the secure transmission of digital images, many new encryption schemes have been proposed. Among them, the problem of encrypted image transmission is particularly important [9,10]. Optical network technology based on fibre optic communication has developed rapidly in recent years, and due to the advantages of efficient transmission in optical networks, it plays an irreplaceable role in the transceiver side of embedded devices [11,12].

However, on the one hand, many such algorithms do not have provable security, and on the other hand, they are less combined with Optical Access Network communication,

which is also an important problem that must be solved in applications [13]. Therefore, it is necessary to study image encryption and transmission technologies based on optical networks. This can show that image encryption and transmission technology based on all-optical networks in the context of the big data era have certain theoretical value and practical significance [14,15].

Throughout the international research status, the research popularity of image encryption technology is increasing, and various encryption methods to enhance the security of algorithms have been proposed [16–20]. In 2020, Ref. [21] proposed cryptanalysis of an image block encryption algorithm based on chaotic maps. Its equivalent secret key can be easily recovered with some chosen plain-images. The summarized security defects can be used to inform designers of image-encryption algorithms about common security pitfalls in the field of image security, particularly chaotic cryptography.

In the same year, Ref. [22] proposed a new image multi encryption algorithm based on HDWT hyper-chaotic system generation, which increased the number of sequence generators and increased the size of the key space exponentially. In the same year, Ref. [23] proposed a novel time-lagged chaotic system, and a novel digital image-encryption algorithm was designed based on this system. The experimental results showed that the algorithm has the advantages of good encryption effect and high system security.

In 2021, Ref. [24] proposed an image-encryption algorithm based on DNA encoding and two specially configured binary chaotic kernels. After the security analysis of the scheme, it was proven that the algorithm can resist known attacks and has excellent encryption performance. In 2022, Ref. [25] re-analysed the theoretical security and practical performance of a medical privacy protection scheme based on DNA en-coding and chaotic maps. Detailed experimental results were provided to show more security defects, including the existence of a large number of weak secret keys, weak key sensitivity, and low efficiency.

The DNA-based encryption scheme that was analysed is important for promoting interdisciplinary research on application of DNA computing in cryptography. Most studies on encryption algorithms have achieved good results [26–29]; however, in the current research, the images are regarded as two-dimensional matrix encryption, which exposes two defects:

(1) Most image encryption is only based on spatial-domain algorithms, and the encryption speed is slower. Compared with the spatial-domain algorithm, the frequency-domain algorithm has higher encryption efficiency. Due to the complexity of the frequency-domain algorithm, it can bring greater deciphering difficulties to illegal decipherers, and the security performance is much higher than that of the spatial-domain algorithm. (2) The system based on chaos is relatively complex. Although it ensures the randomness of chaotic sequences, there are still problems, such as high algorithm redundancy and slow generation of chaotic systems.

Compared with the existing research, this paper proposes a frequency-domain image-encryption algorithm based on two-dimensional chaos and discrete wavelet transform and makes innovative research. First, a dynamic key with plaintext correlation is generated by MD5, and 2D-LASM chaos is generated based on the key to obtain a chaotic pseudo-random sequence. Secondly, the plaintext image is transformed by DWT to map the image from the time domain to the frequency domain and decompose it into low-frequency (LF) coefficient and high-frequency (HF) coefficient.

Then, the chaotic sequence is used to encrypt the LF coefficient with the structure of “confusion-permutation”, and only the HF coefficient is scrambled. The processed LF coefficient and HF coefficient are reconstructed to obtain the frequency-domain ciphertext image. Finally, the ciphertext is dynamically diffused using the chaotic sequence to obtain the final ciphertext. Theoretical analysis and simulation experiments show that the algorithm has a large key space and can effectively resist various attacks.

At the same time, it reduces the burden of channel transmission by reducing the redundancy of image data and ensures the security of image transmission in the public

channel. In addition, combined with the characteristics that wavelet transform is suitable for real-time applications [30], we studied an end-to-end image security system based on Raspberry Pi and transplanted the algorithm to the embedded system equipment to run. The experimental results show that this system can protect user data better in real-time transmission under the transport layer TCP protocol and has good application prospects and research value in the field of information security.

## 2. Related Theory

### 2.1. 2D-Logistic-Adjusted-Sine Map

The chaotic system first proposed by the American meteorologist Lorenz is a nonlinear dynamical system with the characteristics of non-divergence, non-convergence and non-period. Due to the complex dynamics of chaotic systems, the sequences generated by these systems are usually strongly random [31–34]. At the same time, due to the high initial value sensitivity of chaotic systems, the sequences are usually difficult to predict; therefore, chaotic sequences have been widely used in secure communication.

Ref. [35] indicated that the key size of image-encryption algorithms should be at least  $10^{30} \approx 2^{100}$ . Compared with two-dimensional chaotic systems, one-dimensional chaotic systems, such as Logistic and Sine are easy to predict the iterative sequence, have a small key space, and do not have complex chaotic properties. The high-dimensional chaotic systems formed by the combination of low dimensional chaotic systems have more control parameters, and the chaotic structures are more complex. In this paper, we use the 2D-LASM designed by Hua et al. [36] based on the combination of Logistic and Sine mapping chaotic system, which is expressed as

$$\begin{cases} x_{n+1} = \sin(\pi\beta_1(y_n + 3)x_n(1 - x_n)) \\ y_{n+1} = \sin(\pi\beta_2(x_n + 3)y_n(1 - y_n)) \end{cases} \quad (1)$$

where  $x_{n+1}, y_{n+1} \in [0, 1]$  are the pseudo-random sequences generated by chaos and the control parameters  $\beta_1, \beta_2 \in [0, 1]$ . The two input parameters of this chaotic system interact with each other, and output pair  $(x_n + 1, y_n + 1)$  is distributed to the two-dimensional phase plane. Figure 1 is the phase diagram of 2D-LASM. As can be seen from the phase diagram, the output sequence  $(x_i, y_i)$  of the 2D-LASM map covers a large area on a two-dimensional plane.

The 0–1 Gottwald–Melbourne test can determine the regular motion and chaotic motion by calculating the parameter  $k$  asymptotically close to 0 or 1. As shown in Figure 2, the  $k$  value of the average result of 10,000 times is 0.9975, which is close to the theoretical value [37]. This can verify the excellent performance of the chaotic system.

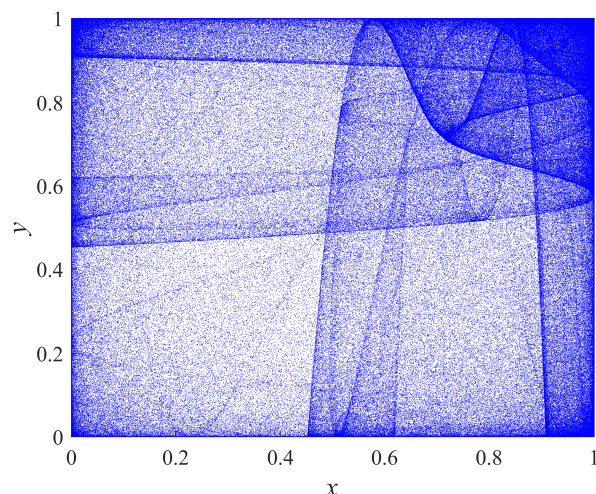


**Figure 1.** Phase diagrams of 2D-LASM with  $\mu = 0.85$ .

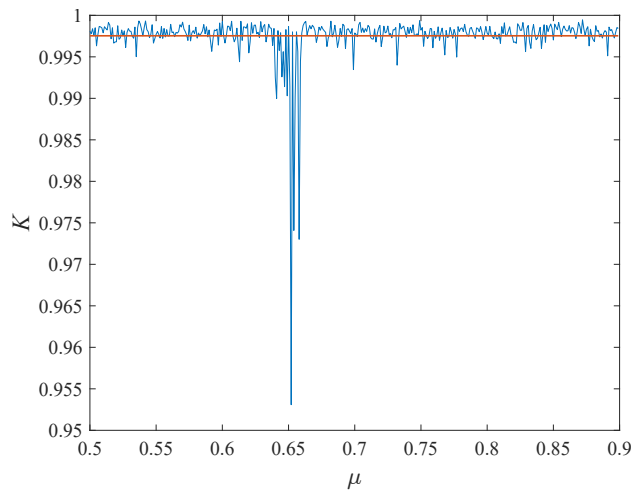


**Figure 2.** The 0–1 Gottwald–Melbourne test.

## 2.2. Discrete Wavelet Transform

Wavelet transform performs multi-scale refinement of signal gradually through scaling and translation operations [38,39], finally achieves time subdivision at high frequency and frequency subdivision at low frequency, and can automatically adapt to the requirements of time–frequency signal analysis.

**Definition 1.** For any  $f(t) \in L^2(\mathbb{R})$ , after the basic wavelet  $\psi(t)$  is shifted by  $b$ , and then the inner product is made with the signal to be analysed  $f(t)$  at different scales  $a$ . The mathematical expression is given by

$$WT_{f(a,b)} = \frac{1}{\sqrt{a}} \int_R f(t)\psi\left(\frac{t-b}{a}\right)dt \quad a, b \in \mathbb{R}, a > 0 \quad (2)$$

where  $a$  is the scale factor, whose role is to stretch the basic wavelet  $\psi(t)$  function,  $b$  is the translation factor, whose value can be positive or negative, and  $a$  and  $b$  are both continuous variables; thus, it is called a continuous wavelet transform.

**Definition 2.** The DWT is to discretize the scale factor  $a$  and the translation factor  $b$  on the basis of the continuous wavelet transform, and turn it into a power series structure,  $a = a_0^j (a_0 \neq 1, j \in \mathbb{Z})$ ,  $b = k a_0^j b_0 (b_0 > 0, k \in \mathbb{Z})$ , the mathematical expression for the 2D-DWT of the image  $f(x,y)$  of size  $M \times N$  is

$$\begin{cases} W_\phi(j_0, a, b) = \frac{1}{\sqrt{MN}} \sum_{x=0}^{M-1} \sum_{y=0}^{N-1} f(x,y) \phi_{j_0,a,b}(x,y) \\ W_\psi^i(j, a, b) = \frac{1}{\sqrt{MN}} \sum_{x=0}^{M-1} \sum_{y=0}^{N-1} f(x,y) \psi_{j,a,b}^i(x,y), i = \{H, V, D\} \end{cases} \quad (3)$$

where  $j_0$  is an arbitrary scale initial value,  $i$  is the superscript of the assumed values  $H$ ,  $V$  and  $D$ ,  $\phi_{j_0,a,b}(x,y)$  represents the scaling function,  $W_\phi(j_0, m, n)$  is  $f(x,y)$  approximate coefficients at the scale  $j_0$ ,  $W_\psi(j, m, n)$  coefficients add detail coefficients in the horizontal, vertical, and diagonal directions for scale  $j \geq j_0$ .

The schematic diagram of the image wavelet decomposition is shown in Figure 3. LL denotes low frequency, HL, LH, and HH denote high frequency, and the subscripts 1 and 2 denote the first-level and second-level decomposition, respectively. The image is decomposed into four sub-images after 2D-DWT: the low-frequency component of the original image, the high-frequency component in the horizontal direction, the high-frequency component in the vertical direction, and the high-frequency component in

the diagonal direction. The low-frequency components continue to be decomposed into sub-images of lower resolution in the next level in exactly the same way.

In this way, the image is decomposed into multiple sub-images at different resolution levels and in different directions, which is consistent with the visual characteristics of the human eye. The schematic diagram of the wavelet decomposition data flow is shown in Figure 4.  $x[n]$  represents the discrete input signal,  $g[n]$  represents the low-pass filter, which is used to retain the low-frequency components of the input signal and remove the high-frequency components,  $h[n]$  represents the high-pass filter, whose function is opposite to that.

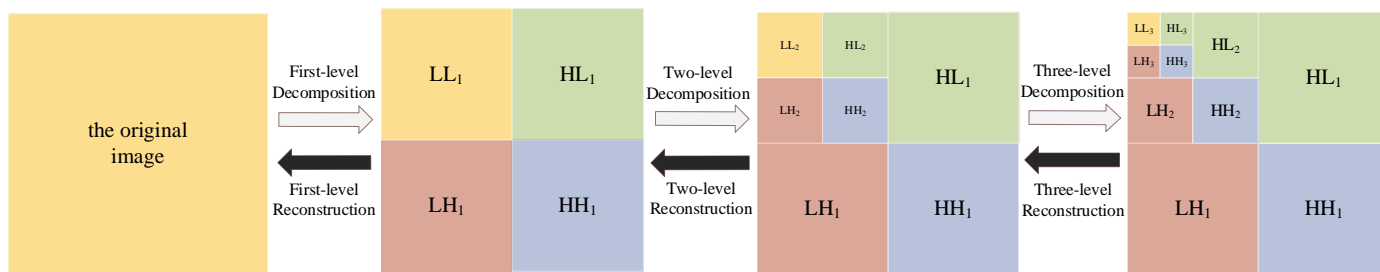


**Figure 3.** Block diagram of the three-level DWT scheme.

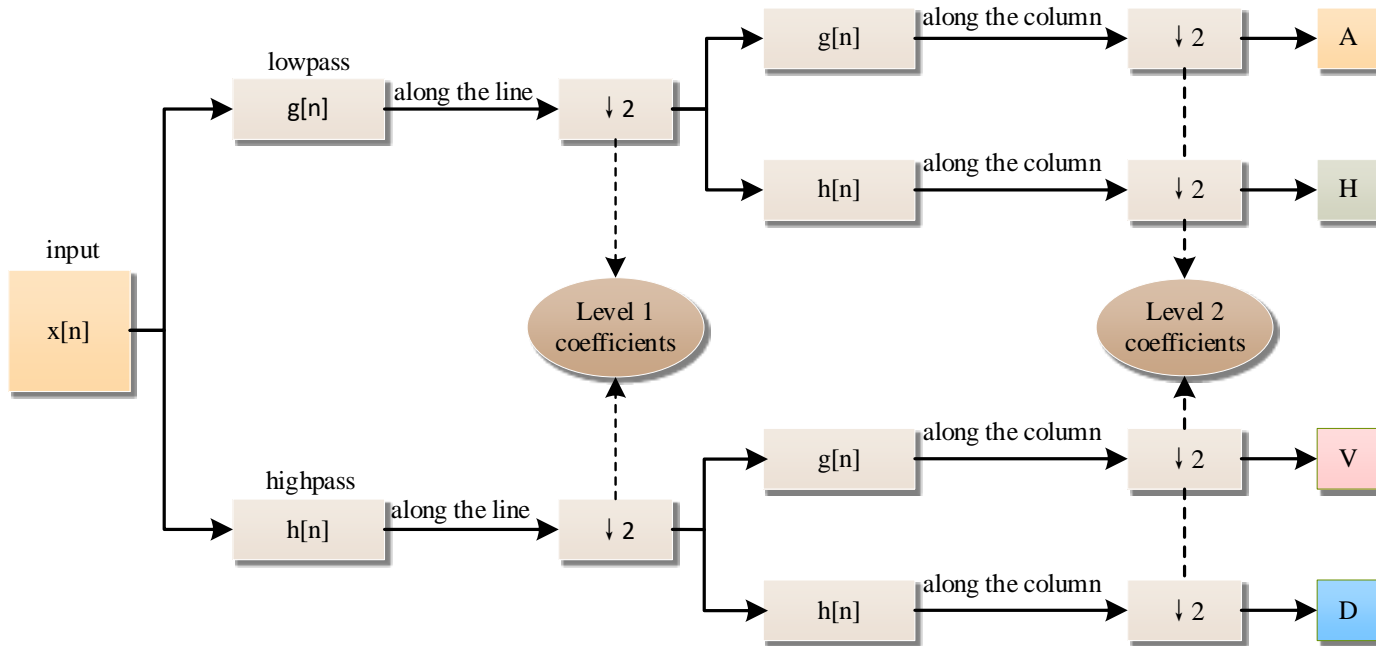


**Figure 4.** Schematic diagram of wavelet decomposition data flow.

The 2D-DWT processing is performed on the  $8 \times 8$  image block by transforming each row of the array, and then transforming each column of the array after the row transformation. Finally the transformed image data array is encoded. The elements in the upper left corner are called low-frequency coefficients, and the remaining elements are called high-frequency coefficients. The data before and after the transformation is shown in Figure 5.

Original Matrix									Transformed Matrix								
64	2	3	61	60	6	7	57		32.5	0	0	0	0	0	0	0	0
9	55	54	12	13	51	50	16		0	0	0	0	0	0	0	0	0
17	47	46	20	21	43	42	24		0	0	0	0	4	-4	4	-4	
40	26	27	37	36	30	31	33		0	0	0	0	4	-4	4	-4	
32	34	35	29	28	38	39	25		0	0	0.5	0.5	27	-25	23	-21	
41	23	22	44	45	19	18	48		0	0	-0.5	-0.5	-11	9	-7	5	
49	15	14	52	53	11	10	56		0	0	0.5	0.5	-5	7	-9	11	
8	58	59	5	4	62	63	1		0	0	-0.5	-0.5	21	-23	25	-27	

**Figure 5.** Data comparison before and after 2D-DWT.

Among them, the data 32.5 of Transformed Matrix is the low-frequency coefficients of the matrix, which shows that the energy of the image is mainly concentrated in the low-frequency coefficients after 2D-DWT. Based on this, only the low-frequency coefficients in the frequency domain after DWT need to be encrypted to obtain a more satisfactory image encryption effect.

### 3. Design of Encryption Algorithm

In traditional encryption algorithms, they are often designed for one-dimensional data stream information, the drawbacks of which are high computational complexity and low encryption efficiency, which are slightly stretched for digital images with large data volume, spatial order, strong correlation, and high redundancy. In particular, with the development of technology, the information contained is even gradient increasing. Therefore, this paper proposes an image-encryption algorithm based on DWT and a 2D-LASM chaotic system and introduces a dynamic key with plaintext correlation to achieve “one-time pad” encryption, and the specific process of encryption and decryption is shown in Figure 6. The specific encryption algorithm is designed as follows.

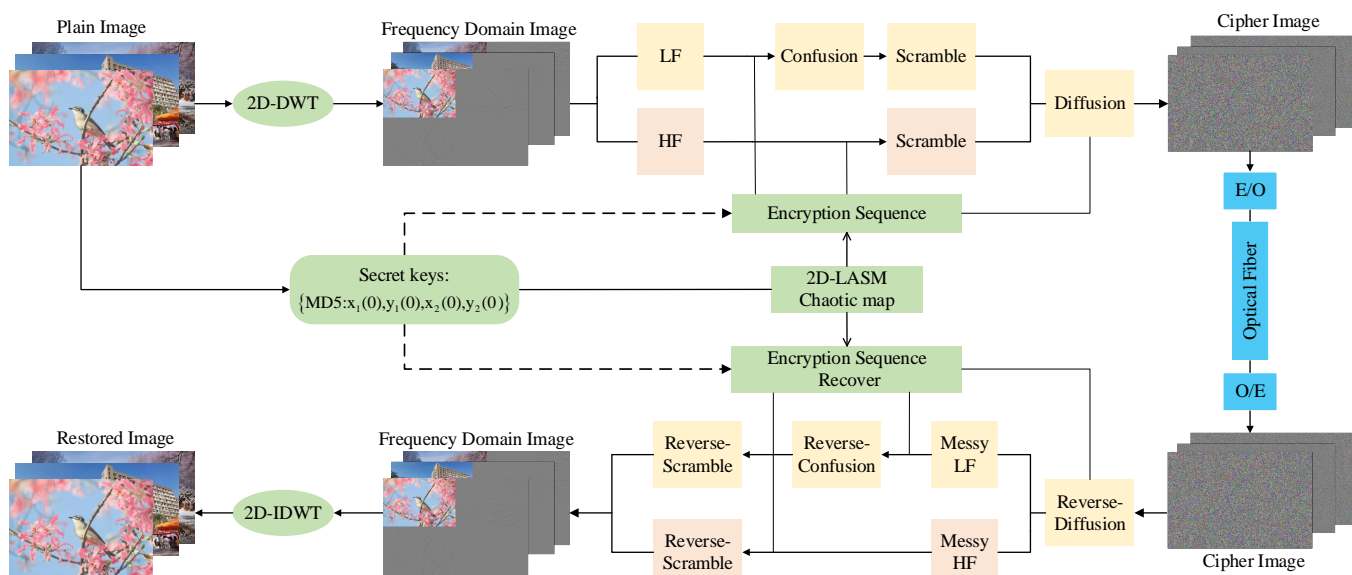


**Figure 6.** Principles and mechanisms of image encryption and decryption.

#### Step 1: Use 2D-DWT to decompose plaintext images

The image is decomposed of DWT into four subbands:  $LL$ ,  $LH$ ,  $HL$ , and  $HH$ , are performed according to Equation (4), and the coefficients of each subband are calculated using a Haar filter to map the image matrix from the spatial domain to the frequency

domain. Then, the data is processed into the pixel value range of 0–255 to obtain one low-frequency image and three high-frequency images. The specific treatment is shown as

$$\begin{cases} LL(x, y) = \frac{p(x, y) + p(x, y+1) + p(x+1, y) + p(x+1, y+1)}{2} \\ LH(x, y) = \frac{p(x, y) + p(x, y+1) - p(x+1, y) - p(x+1, y+1)}{2} \\ HL(x, y) = \frac{p(x, y) - p(x, y+1) + p(x+1, y) - p(x+1, y+1)}{2} \\ HH(x, y) = \frac{p(x, y) - p(x, y+1) - p(x+1, y) + p(x+1, y+1)}{2} \end{cases} \quad (4)$$

where  $p(x, y)$ ,  $p(x, y + 1)$ ,  $p(x + 1, y)$ , and  $p(x + 1, y + 1)$  are the four pixel points of the  $LL$ ,  $LH$ ,  $HL$ , and  $HH$ .

### Step 2: Pseudo-random sequence preprocessing

The key of this algorithm consists of the MD5 value of the plaintext image, the initial value of the 2D-LASM chaos, and the control parameters. MD5 can scramble the initial values of the chaotic system to make the key sequence more sensitive to the plaintext, thus, enhancing the security of the algorithm. The detail of this algorithm is shown as

$$\begin{cases} x'_1(0) = x_1(0) + (m_1 \oplus m_2 \oplus m_3 \oplus m_4) / 256 \\ y'_1(0) = y_1(0) + (m_5 \oplus m_6 \oplus m_7 \oplus m_8) / 256 \\ x'_2(0) = x_2(0) + (m_9 \oplus m_{10} \oplus m_{11} \oplus m_{12}) / 256 \\ y'_2(0) = y_2(0) + (m_{13} \oplus m_{14} \oplus m_{15} \oplus m_{16}) / 256 \end{cases} \quad (5)$$

where  $\oplus$  is a bitwise XOR operation,  $x_1(0)$ ,  $y_1(0)$ ,  $x_2(0)$ , and  $y_2(0)$  are two groups of initial values of 2D-LASM chaotic system.  $x'_1(0)$ ,  $y'_1(0)$ ,  $x'_2(0)$ , and  $y'_2(0)$  are two groups of initial values updated after the disturbance from MD5. Clearly, the new initial values will change with different plaintext images. The confusion sequence is generated by

$$\begin{cases} L = H \times W \times Ch \\ L_d = L / 2 \\ R = [x_1(1 : L_d); y_1(1 : L_d)] \end{cases} \quad (6)$$

where  $R$  is composed of two chaotic sequences obtained by the initial value solution of 2D-LASM. The length of  $R$  is the same as  $L$ ,  $H$  and  $W$  are the pixel rows and columns of the plaintext image to be encrypted, and  $Ch$  is the number of channels of the plaintext image to be encrypted. A complete colour image is composed of three channels of red, green, and blue, while a greyscale image requires only one channel. The mask obfuscation sequence is generated by

$$\begin{cases} R'_c = \text{flood}(\text{mod}(R \times 10^{10}, 256)) \\ R_c = \text{reshape}(R'_c, H, W) \end{cases} \quad (7)$$

where  $\text{floor}(\ast)$  is a downward rounding operation;  $\text{mod}(\ast)$  is a remainder function whose result is the remainder obtained by dividing two numerical expressions;  $\text{reshape}(\ast)$  is a reshaping function generated  $R_c$  for the mask obfuscation operations, which is a sequence of integers with value range  $\in [0, 255]$ , and its length is  $H \times W$ . The pixel scrambling sequence is generated by

$$\begin{cases} seq\_H = x_2(1 : H) \\ seq\_W = y_2(2, 1 : 8 \times W) \\ [S_1, R_{pr}] = sort(seq\_H) \\ [S_2, R_{pc}] = sort(seq\_W) \end{cases} \quad (8)$$

where  $sort(*)$  is the equation that sorts all elements of the sequence;  $seq\_H$  denotes the chaos-based length sequence extracted from  $x_1$ ;  $seq\_W$  denotes the chaotic sequence of length  $8 \times W$ , extracted from  $y_2$ ;  $R_{pr}$  denotes a pixel row generated by the sorting function and length  $H$ ;  $R_{pc}$  denotes a pixel column generated by the sorting function with length  $8 \times W$ ; and  $S_1$  and  $S_2$  are chaos-based sorted sequence values. The diffusion sequence is generated by

$$\begin{cases} R_{d1} = flood(mod(R \times 10^8, 256)) \\ R_{d2} = flood(mod(R \times 10^9, 256)) \end{cases} \quad (9)$$

where the lengths of  $R_{d1}$  and  $R_{d2}$  are  $H \times W$ . The  $R_{d1}$  and  $R_{d2}$  sequences are used for dynamic diffusion operations.

### Step 3: Confusion

The ordinary image  $P$  is blurred with the confusion sequence  $R_c$  so that the image can obtain the blurred image  $C_1$  by hiding—namely,

$$C_1(i) = R_c(i) \oplus P(i), i = (1, 2, \dots, L) \quad (10)$$

### Step 4: Pixel permutation

The blurred image  $C_1$  is encrypted by pixel dislocation using the dislocation sequence  $R_{pc}(i)$  and  $R_{pr}(j)$  to obtain image  $C_3$ —namely,

$$\begin{cases} C_2 = swap(C_1(:, R_{pc}(i)), C_1(:, i)) \\ C_3 = swap(C_2(:, R_{pr}(j)), C_1(j, :)) \end{cases} \quad (11)$$

where  $i = 1, 2, \dots, H; j = 1, 2, \dots, 8 \times W$ ;  $C_2$  is the image after the double-bit column transformation arrangement;  $C_3$  is the image after the double-bit row transformation arrangement; and  $swap(*)$  is used to exchange the values of two pixels.

### Step 5: Dynamic diffusion

Dynamic diffusion allows each pixel to interact with each other, thus achieving an avalanche effect. By establishing a diffusion path between pixels and adding keys  $R_{d1}$  and  $R_{d2}$  to the diffusion process, the ciphertext pixels are diffused along that path to other pixels to generate the final ciphertext image  $C$ .

The diffusion encryption generation equation for the first greyscale pixel  $C(1)$  of the ciphertext image  $C$  is shown as

$$\begin{cases} sum(1) = \sum_{i=1}^L C_3(i) \\ C(1) = C_3(1) \oplus R_{d1}(1) \oplus (sum(1) \dotplus R_{d2}(1)) \end{cases} \quad (12)$$

where the operator  $\dotplus$  can be defined as  $c \dotplus d \triangleq mod(c + d, 256)$ ;  $C_3(1)$  is the first pixel in the replacement image  $C_3$ ;  $R_{d1}(1)$  and  $R_{d2}(1)$  are the first elements of the diffusion encryption

sequence; and  $sum(1)$  represents the accumulation of all pixels of the replacement image  $C_3$  and then generates the ciphertext pixel  $C(i)$ —namely,

$$\begin{cases} C(i) = C_3(i) \oplus (C(i-1) + R_{d1}(i) \oplus (sum(i) + R_{d2}(i))) \\ sum(i) = sum(i-1) - C_3(i) \end{cases} \quad (13)$$

where  $i = 2, 3, \dots, L$ ;  $i$  denotes the  $i$ th pixel of image  $C_3$  after remodelling;  $C(i-1)$  is the  $(i-1)$ th ciphertext pixel of the sequence of pixels representing dynamic diffusion encryption greyscale; and  $sum(i)$  is the cumulative sum of  $(L-i)$  pixel values of image  $C_3$ . According to Equation (13), starting from the second ciphertext pixel  $C(2)$ , the cipher image  $C$  is generated by computing  $C(i)$  through iterations of  $i$  in  $\{1, 2, \dots, L\}$ , until the  $L$ th ciphertext pixel  $C(L)$  is generated.

## 4. Experimental Verification and Discussion

### 4.1. Performance Analysis of the Image-Encryption Algorithm

The image-encryption algorithm proposed in this paper is based on the MATLAB r2018b system to complete the verification analysis. The system ran on a Windows 10 64-bit operating system, Intel(R) Core(TM) I7-6500U CPU @ 2.50 GHz 2.59 GHz processor and 8 GB memory running on a PC. This article selected some standard images as the test images for experiments, and most of the test images were from the “USC-SIPI Image Database [40]”.

#### 4.1.1. Key Space Analysis

The key space refers to the set of all possible keys that can be used to generate the key. The size of the key space depends on the length of the security key, which is one of the most important characteristics in determining the strength of a cryptosystem. The image-encryption algorithm designed in this paper uses a two-dimensional discrete chaotic system, and the key parameters involved are four chaotic initial values  $x_1(0), y_1(0), x_2(0)$ , and  $y_2(0)$ . The calculation accuracy of 64-bit double precision is  $2^{15}$ . The size of the key space of this part is  $10^{15} \times 10^{15} \times 10^{15} \times 10^{15} = 10^{60} \approx 2^{199}$ .

Considering that the introduced MD5 can output 128-bit hash value, the key space of this encryption scheme is calculated as  $2^{327}$ , and the key length reaches 327 bits. From Table 1, it can be seen that the key space of this paper has obvious advantages compared with other existing encryption schemes, the key space of this paper has clear advantages. Therefore, the encryption algorithm in this paper can resist any form of brute force attack [41].

**Table 1.** Key space size comparison table.

	This Article	Ref. [42]	Ref. [43]
Key space/bits	327	128	309

#### 4.1.2. Histogram Analysis

The colour histogram is an important feature of the statistical properties of an image, with the horizontal coordinate indicating the pixel value and the vertical coordinate indicating how often the pixel appears in the image. The ideal encryption algorithm should result in different plaintext images having a uniform statistical distribution or a similar histogram that is independent of the plaintext image [44]. From Figure 7, we know that, although the histograms of the plaintext images are completely different, the histograms of the ciphertext images all have similar distribution characteristics, indicating that the algorithm has a strong resistance to statistical attacks.

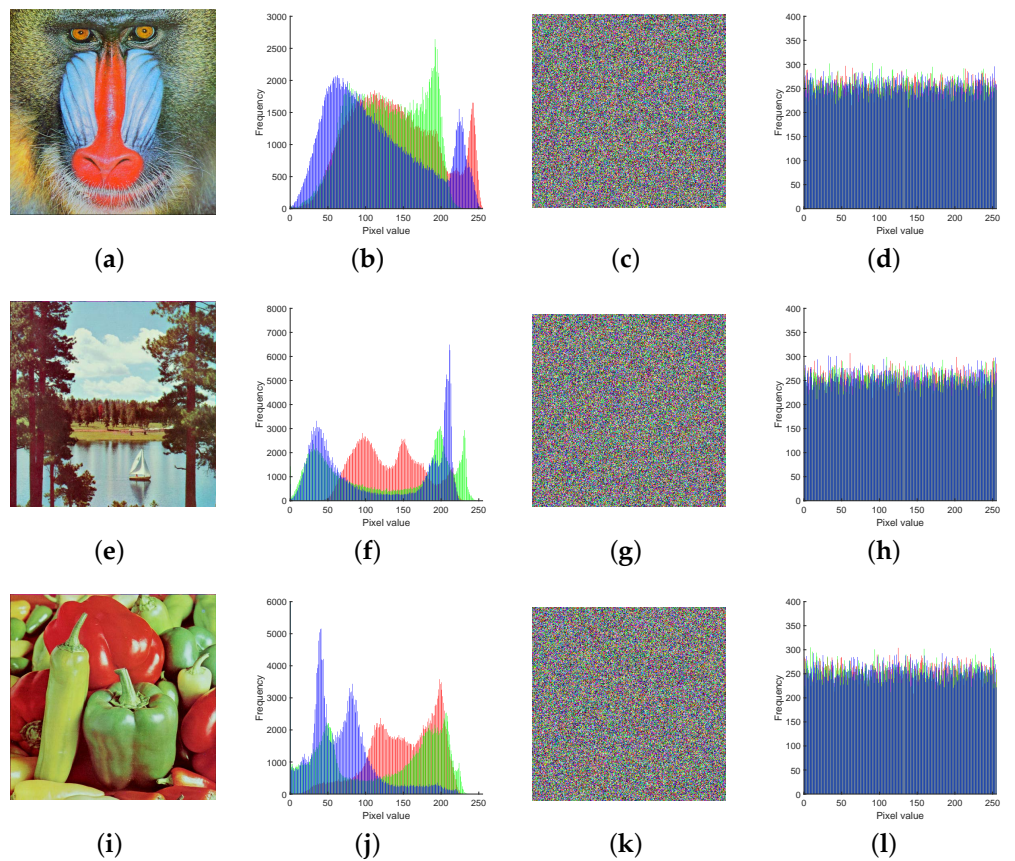


**Figure 7.** Histogram of images before and after encryption: (a) Plaintext image of “4.2.03.tif”; (b) Histogram of the plaintext image of (a). (c) Ciphertext image of (a). (d) Histogram of the ciphertext image of (a). (e) Plaintext image of “4.2.06.tif”. (f) Histogram of the plaintext image of (e); (g) Ciphertext image of (e). (h) Histogram of the ciphertext image of (e). (i) Plaintext image of “4.2.07.tif”. (j) Histogram of the plaintext image of (i). (k) Ciphertext image of (i). (l) Histogram of the ciphertext image of (i).

#### 4.1.3. Coefficient of Adjacent Pixels

Every image has intrinsic and inherent characteristics, such as high pixel correlation and high redundancy [45]. Correlation analysis tests the strength of the correlation between image pixels, and the correlation between neighbouring pixels of a normal image is usually high, with a correlation coefficient closer to 1. At the same time, a secure and efficient encryption algorithm must satisfy the requirement of a low correlation coefficient between neighbouring pixels of a ciphertext image in order to resist statistical attacks. The correlation coefficient can be calculated from Equation (14)—namely,

$$\begin{cases} E(x) = \frac{1}{N} \sum_{i=1}^N x_i \\ D(x) = \frac{1}{N} \sum_{i=1}^N (x_i - E(x))^2 \\ cov(x, y) = \frac{1}{N} \sum_{i=1}^N (x_i - E(x))(y_i - E(y)) \\ \gamma_{xy} = \frac{cov(x,y)}{\sqrt{D(x)} \times \sqrt{D(y)}} \end{cases} \quad (14)$$

where the grey scale value of each pixel is denoted by  $x$  and  $y$ , respectively,  $E(x)$  denotes the mean value,  $D(x)$  denotes the variance,  $cov(x, y)$  denotes the covariance, and  $\gamma_{xy}$  denotes the correlation coefficient. Table 2 shows the encryption quality of the proposed scheme and the classic encryption schemes in recent years. We evaluate the correlation between

adjacent pixels in horizontal, vertical, and diagonal directions, as shown in Figure 8, from which it can be inferred that the correlation between adjacent pixels of the password is not strong. Therefore, from the experimental results, it can be found that the encryption algorithm in this paper can effectively resist statistical analysis [46].

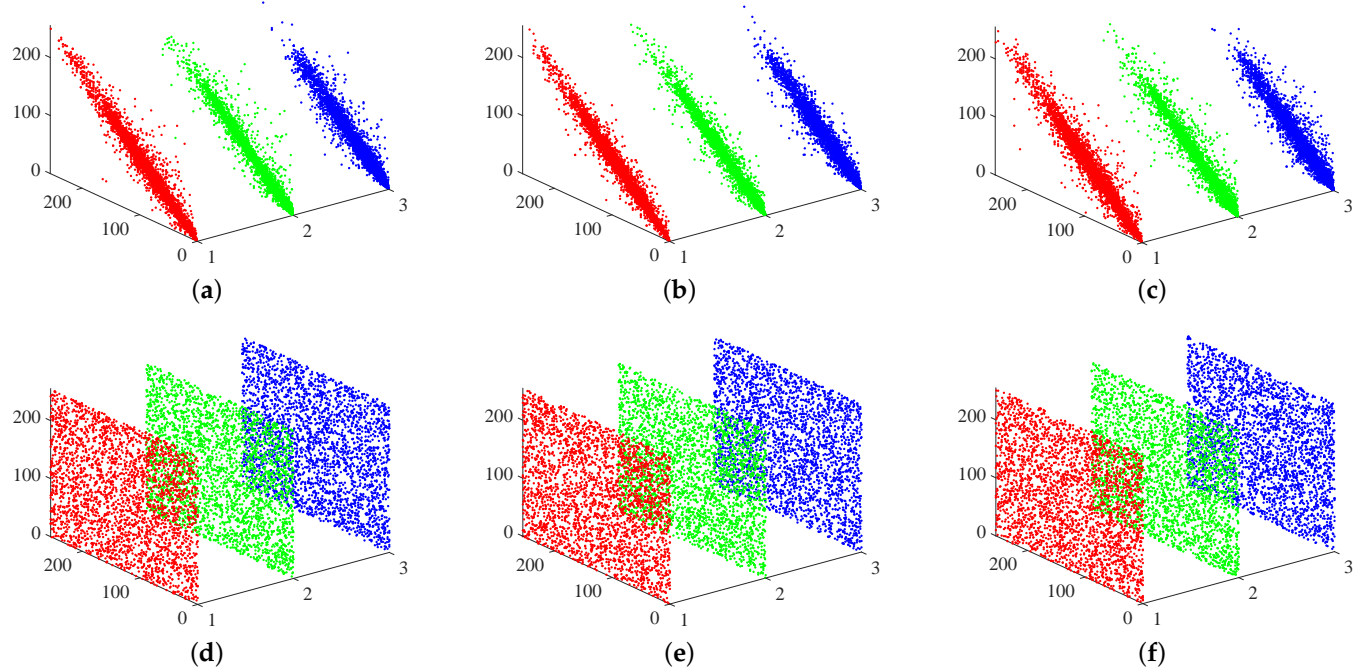


**Figure 8.** Correlation coefficients distribution map of plain image and ciphered image of “4.1.01.tiff”: (a) Correlation of “4.1.01.tiff” in the horizontal direction. (b) Correlation of “4.1.01.tiff” in the vertical direction. (c) Correlation of “4.1.01.tiff” in the diagonal direction. (d) Correlation of ciphered “4.1.01.tiff” in the horizontal direction. (e) Correlation of ciphered “4.1.01.tiff” in the vertical direction. (f) Correlation of ciphered “4.1.01.tiff” in the diagonal direction.

**Table 2.** Comparison results of the correlation coefficients of adjacent pixels.

Component	Direction	Original Images	Algorithm in This Paper	Ref. [47]	Ref. [48]	Ref. [9]
R	Horizontal	0.9736	-0.0215	-0.0063	0.0076	0.0023
	Vertical	0.934	-0.0219	-0.0016	0.0017	-0.0130
	Diagonal	0.934	0.0082	0.00156	0.0110	-0.0061
G	Horizontal	0.96	0.0272	-0.0032	-0.0048	-0.0236
	Vertical	0.9346	0.0263	0.0335	0.0274	0.0308
	Diagonal	0.9419	0.005	-0.0095	0.0342	-0.0179
B	Horizontal	0.9624	0.0286	-0.0044	-0.0056	-0.0266
	Vertical	0.9213	-0.0489	-0.0079	0.0150	-0.0057
	Diagonal	0.8979	0.0155	0.0034	-0.0115	0.0378

#### 4.1.4. Analysis of Differential Attacks

A complete encryption system should have a high sensitivity to images. The plaintext sensitivity can be one of the main indicators of the security of an encryption system and

the strength of a cryptographic management system against differential attacks. Both the Number of Pixels Change Rate (*NPCR*) and the Unified Average Changing Intensity (*UACI*) can be used to represent the difference between two images that change only on the same pixel [49]. The formula of *NPCR* and *UACI* is defined by

$$\begin{cases} NPCR = \frac{1}{H \times W} \times \sum_{i=1}^H \sum_{j=1}^W D(i, j) \times 100\% \\ UACI = \frac{1}{H \times W} \times \sum_{i=1}^H \sum_{j=1}^W \frac{|v_1(i, j) - v_2(i, j)|}{255} \times 100\% \\ D(i, j) = \begin{cases} 0, v_1(i, j) = v_2(i, j) \\ 1, v_1(i, j) \neq v_2(i, j) \end{cases} \end{cases} \quad (15)$$

where  $v_1(i, j)$  denotes the pixel value of a ciphertext pixel before it is changed; and  $v_2(i, j)$  denotes the pixel value of a ciphertext image after changing the pixel value at a point in the plaintext image. We compare the values of *NPCR* and *UACI* in this paper with other works in Table 3. In addition, the values of *NPCR* and *UACI* after 50 experiments are shown in Figure 9. The *NPCR* and *UACI* average values are near the theoretical value; thus, the encryption algorithm in this paper is sensitive to the pixel changes in the plaintext image. Therefore, the encryption algorithm designed in this paper can effectively resist differential attacks.

**Table 3.** Differential attack analysis.

Images	NPCR(%)				UACI(%)			
	This Paper	Ref. [47]	Ref. [48]	Ref. [9]	This Paper	Ref. [47]	Ref. [48]	Ref. [9]
4.2.06.tiff [40]	99.6758	99.6188	99.6269	99.6033	33.4371	24.8663	27.9449	32.2283
4.2.03.tiff [40]	99.8474	99.6081	99.6189	99.6057	33.5871	29.9629	29.9636	29.9411
7.1.02.tiff [40]	99.8426	99.6020	99.5995	99.6132	33.4306	29.3349	29.3636	29.3176
2.2.03.tiff [40]	99.6282	99.6172	99.6072	99.6144	33.4007	31.2027	27.6087	31.2021

#### 4.1.5. Image Quality Analysis

The Peak Signal-to-Noise Ratio (*PSNR*) and Structural SIMilarity (*SSIM*) are commonly used in the field of image processing as a tool to weigh the quality of encryption. The Mean Square Error (*MSE*) is a part of *PSNR* and is defined by

$$\begin{cases} MSE = \frac{1}{H \times W} \sum_{i=1}^H \sum_{j=1}^W (X(i, j) - Y(i, j))^2 \\ PSNR = 10 \times \log_{10}(\frac{Q^2}{MSE}) \end{cases} \quad (16)$$

where *MSE* denotes the mean square error of the plaintext image *X* and the ciphertext image *Y*. The height and width of the image are denoted by *H* and *W*, respectively, and *Q* denotes the pixel level of the image. *SSIM* is a measure of the similarity of two images and is defined by

$$SSIM(X, Y) = \frac{(2\mu_X\mu_Y + (0.01L)^2)(2\sigma_{XY} + (0.03L)^2)}{(u_X^2 + u_Y^2 + (0.01L)^2)(\sigma_X^2 + \sigma_Y^2 + (0.03L)^2)} \quad (17)$$

where  $\mu_X, \mu_Y$  denote the mean of image *X* and *Y*, respectively,  $\sigma_X, \sigma_Y$  denote the standard deviation of image *X* and *Y*, respectively, and *L* denotes the dynamic range of pixel values. The values of *PSNR* and *SSIM* are calculated by using Equations (16) and (17) as shown in

**Table 4.** The experimental results show that the *PSNR* and *SSIM* values obtained by this algorithm are low. Therefore, this encryption scheme has certain advantages.

**Table 4.** Image quality analysis.

Images	Original Image and Ciphered Image			Original Image and Restored Image	
	PSNR(dB)	MSE	SSIM	PSNR(dB)	MSE
4.1.07.tiff [40]	25.6436	177.3049	0.0106	39.6267	7.0862
5.1.11.tiff [40]	25.5066	182.9874	0.011	39.593	7.1413
5.1.13.tiff [40]	24.6653	222.0984	0.0064	38.3199	11.418

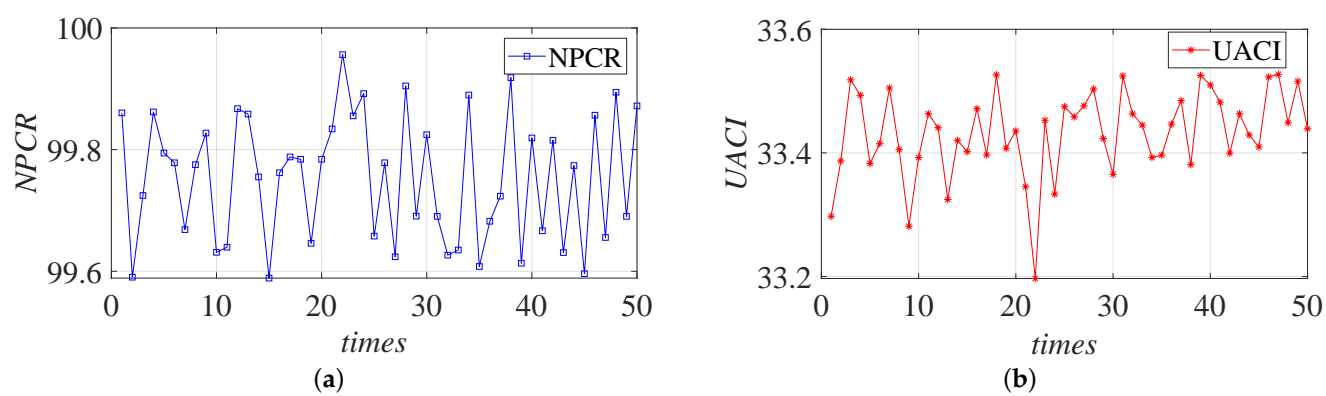


**Figure 9.** NPCR (a,b) values obtained from 50 experiments.

#### 4.1.6. Sensitivity Analysis

In image encryption, key sensitivity performance is often used as an important indicator to measure the security of an encryption system. The key sensitivity is generally expressed by the difference between corresponding images when decrypting or encrypting the same image with a slightly different key. In order to test the sensitivity to the key in the scheme, we processed the two chaotic series by means of time series and compared the generated two-dimensional chaotic series. It can be seen from Figure 10 that the encryption system designed in this paper has high security and strong sensitivity to keys, which increases the difficulties for attackers to decipher the ciphered image.

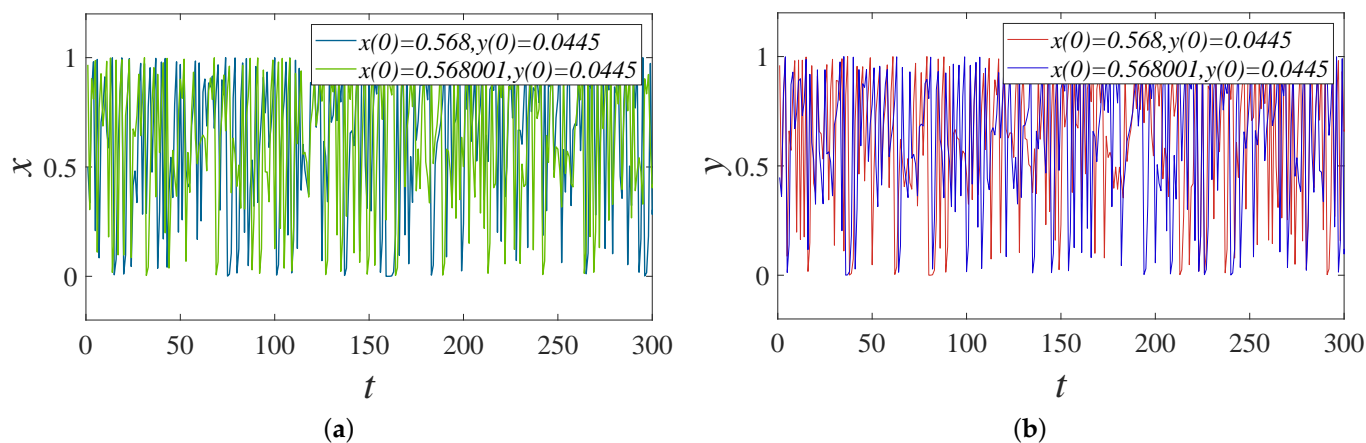


**Figure 10.** Key sequence sensitivity timing diagram: (a) Comparison *x* before and after *x(0)* key perturbation. (b) Comparison *y* before and after *x(0)* key perturbation.

#### 4.1.7. Information Entropy

Information entropy is an indicator of the amount and uncertainty of information contained in digital images. The information entropy of the image is positively correlated with the encryption effect. The larger the information entropy is, the better effect the encryption will have. The formula of information entropy is defined by

$$H(n) = - \sum_{i=1}^L P(n_i) \log_2 P(n_i) \quad (18)$$

where  $i$  represents the pixel greyscale value, and  $P(i)$  represents the probability that this grey value will appear in the digital image. From the calculation of Equation (18), the theoretical value of information entropy is the maximum value of 8. We compare the information entropy of the images before and after encryption, and the experimental result is shown in Table 5. It can be seen that the information entropy of the two ciphertext images is above 7.9994, which has a certain improvement compared with the similar references.

**Table 5.** Image information entropy.

Images	R	G	B
Original image	7.5549	7.0167	6.7347
Ciphertext image in this paper	7.9994	7.9994	7.9993
Ref. [47]	7.9993	7.9994	7.9994
Ref. [48]	7.9992	7.9993	7.9992
Ref. [9]	7.9993	7.9993	7.9993

#### 4.1.8. Efficiency Analysis

There are many factors that can affect the efficiency, such as the size of the image, the degree of arithmetic power consumed by the encryption operation. We selected the images with sizes of  $256 \times 256$ ,  $512 \times 512$ , and  $1024 \times 1024$  for comparison [50]. As shown in Table 6, when the image size becomes larger, the required encryption and decryption time will increase accordingly. From the experimental results, it can be seen that the algorithm has high encryption efficiency.

**Table 6.** Encryption time comparison.

Images	Encryption Time (s)	Decryption Time (s)
4.1.01.tiff ( $256 \times 256$ )	0.599185	0.078700
4.2.03.tiff ( $512 \times 512$ )	0.417543	0.199085
2.2.02.tiff ( $1024 \times 1024$ )	1.239165	0.707843
2.2.03.tiff ( $1024 \times 1024$ )	1.168449	0.646701

#### 4.2. Embedded Hardware Implementation of Image Encryption in Optical Access Network

The image encryption system can also be effectively applied in the optical access network communication scenario, which is illustrated in Figure 11. In this scenario, both the sender and the receiver are embedded terminals for reading and displaying, sending and receiving, and encrypting and decrypting images. In order to enhance the security of the information, we use the optical fibre transmission method to replace the traditional ordinary information transmission method, which greatly enhances the information transmission

process while ensuring real-time performance. The possibility of protection from dangerous elements during information transmission is greatly enhanced. Therefore, the encryption method that we propose is suitable for secure communication in an optical access network environment.

To verify the effectiveness and feasibility of the image encryption system, we conducted experimental analysis on an experimental platform of optical access network based on ARM embedded system. The security, encryption speed, resource utilisation, and cracking difficulty of hardware encryption are all greatly superior to software encryption. The optical access network-based digital image encryption communication system consists of two ARM chip-based embedded development boards and a Gigabit single-mode single-fibre transceiver, TP-LINK TL-FC311A-3.

The maximum transmission distance is approximately 10 km and the maximum transmission rate is above 155 Mbit/s. The ARM development board is the Raspberry Pi 4B, and the programming language used is Python. The chip is a Broadcom BCM2711 with Cortex-A72 architecture, and the operating system is 32-bit Linux 5.4 with a 3.5-inch liquid crystal display (LCD). The wireless router is used for network communication between the sender and the receiver and obtains the sending and receiving addresses via Dynamic Host Configuration Protocol (DHCP), 192.168.1.114 and 192.168.1.115, respectively.

The sender is responsible for reading, displaying, encrypting, and transmitting the plaintext images, while the receiver is responsible for receiving, displaying, and decrypting the corresponding ciphertext images. The experimental platform and results are shown in Figures 12 and 13.

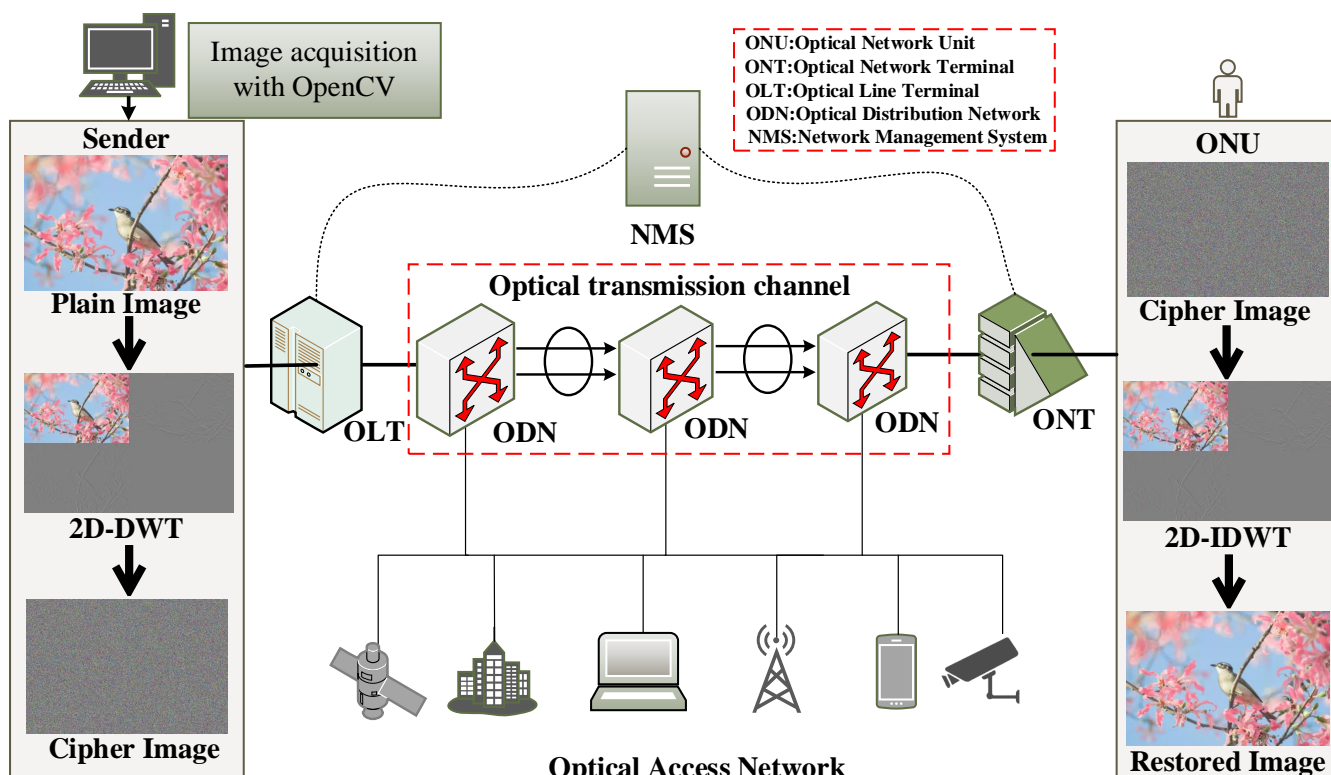


**Figure 11.** Embedded implementation of image wavelet transform encryption used in an Automatic Switched Optical Network.

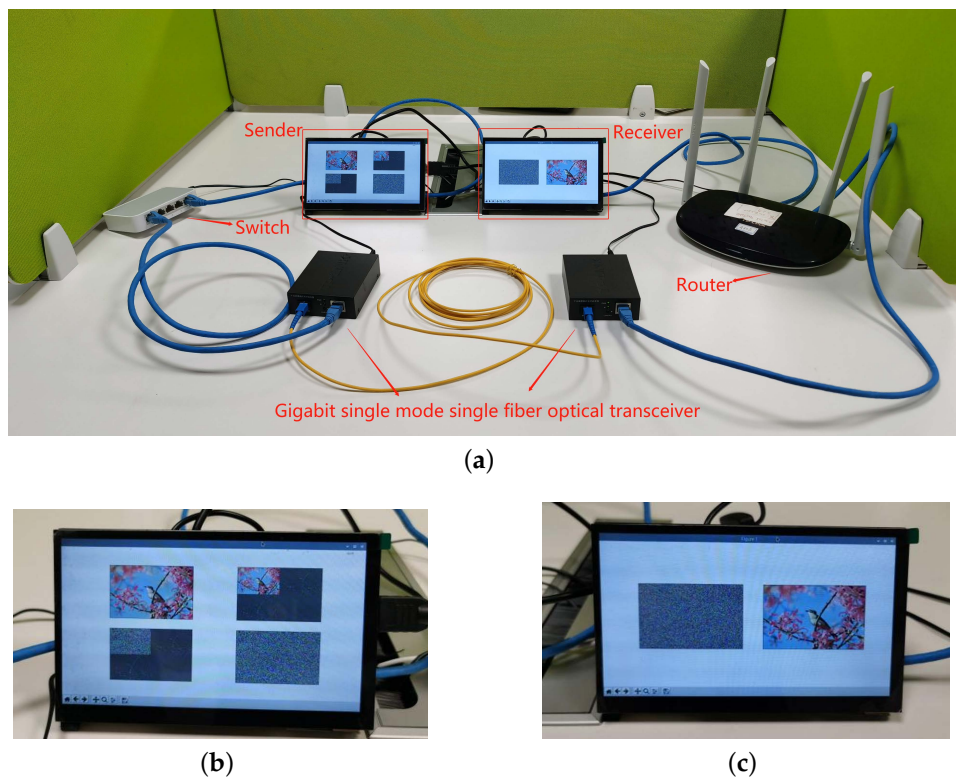


**Figure 12.** Experimental results in an Automatic Switched Optical Network secure communication platform: (a) The overall physical diagram. (b) Image encryption. (c) Decryption image of (b).

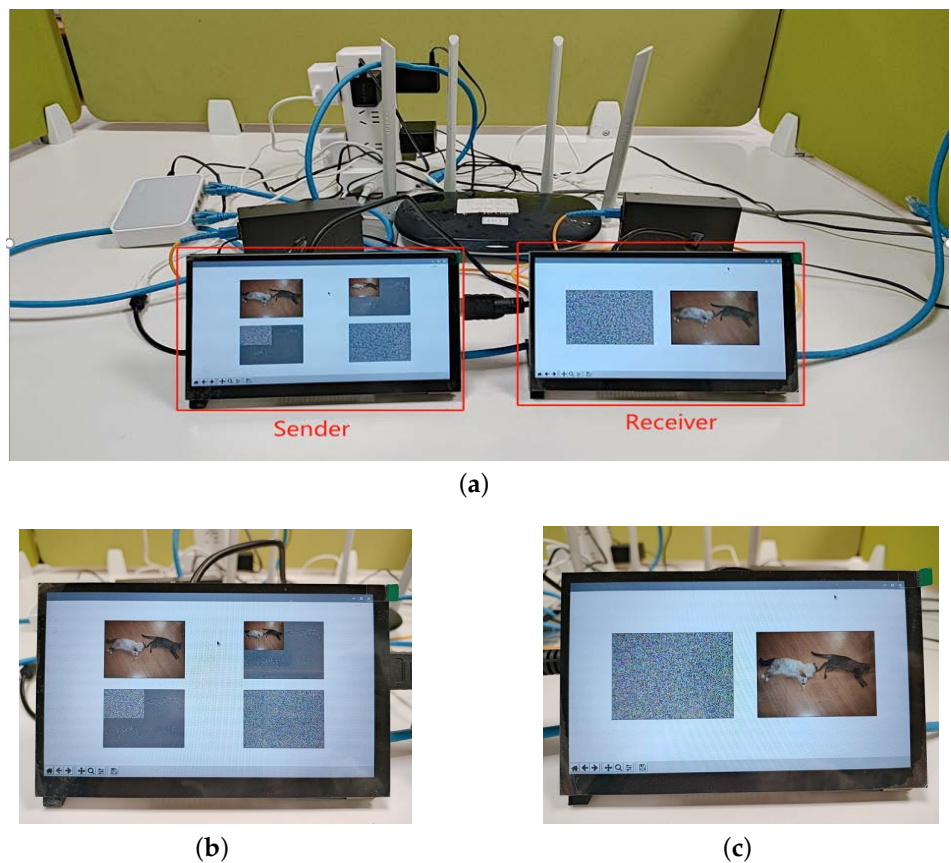


**Figure 13.** Experimental results in an Automatic Switched Optical Network secure communication platform: (a) The overall physical diagram. (b) Image encryption. (c) Decryption image of (b).

## 5. Conclusions

This paper proposed an image encryption scheme based on 2D-LASM and DWT and completed corresponding embedded hardware experiments. To enhance the security performance, we designed an MD5 plaintext association mechanism for obtaining dynamic chaotic sequences to resist the chosen plaintext attacks. In terms of specific encryption operations, we first performed Discrete Wavelet Transform (DWT) on the plaintext image to decompose low-frequency (LF) coefficients and high-frequency (HF) coefficients and encrypted them in different ways according to the weights.

Then, we used the chaotic sequences to perform dynamic diffusion operations on the reconstructed intermediate ciphertext frequency-domain image to obtain the final cipher image. Furthermore, the proposed encryption algorithm was successfully tested in an embedded optical access network communication environment. Theoretical analysis and simulation experiments showed that the algorithm has the characteristics of large key space, excellent statistical analysis performance and the ability to resist various common attacks.

Although the frequency processing is relatively complicated, the encryption algorithm still has the advantages of easy implementation and high efficiency. At the same time, its successful implementation on embedded devices in the optical network environment demonstrated that the algorithm has certain practicability in an Internet-of-Things environment.

**Author Contributions:** Conceptualization, H.W. and C.Z.; Data curation, L.M. and Y.L.; Formal analysis, L.L.; Investigation, S.L. and R.L.; Methodology, Z.C.; Software, J.Z.; Validation, W.L.; Writing—original draft, Z.L.; Writing—review and editing, Y.H., J.Y. and H.Y. All authors have read and agreed to the published version of the manuscript.

**Funding:** This work was supported in part by the National Science Foundation of China under Grant 62071088; in part by the Science and Technology Projects of Guangdong Province under Grant 2021A0101180005; in part by the Special Projects for Key Fields of the Education Department of Guangdong Province under Grant 2021ZDZX1083; in part by the Project for Zhongshan Science and Technology under Grant 2021B2062; in part by the Construction Project of Professional Quality Engineering in Guangdong Province under Grant YLZY202201; in part by the Project of Administration, School and Enterprise of DongGuan Polytechnic under Grant ZXD202215; in part by the Special Projects in Key Fields of Research Platforms and Projects of Guangdong Universities (2022ZDZX3082); in part by Dongguan Science and Technology Commissioner Project (20221800500572); and in part by the Special Fund for Electronic Information Engineering Technology Specialty Group of National Double High Program of Dongguan Polytechnic (ZXD202215).

**Institutional Review Board Statement:** Not applicable.

**Informed Consent Statement:** Not applicable.

**Data Availability Statement:** Data sharing not applicable to this article as no datasets were generated during the current study.

**Conflicts of Interest:** The authors declare that they have no conflicts of interest. The manuscript was written through contributions of all authors. All authors have given approval on the final version of the manuscript.

## References

1. Cui, M.; Zhang, C.; Chen, Y. Multilayer Dynamic Encryption for Security OFDM-PON Using DNA-reconstructed Chaotic Sequences under Cryptanalysis. *IEEE Access* **2021**, *9*, 18052–18060. [[CrossRef](#)]
2. Masood, F.; Ahmad, J.; Shah, S. A Novel Hybrid Secure Image Encryption Based on Julia Set of Fractals and 3D Lorenz Chaotic Map. *Entropy* **2020**, *22*, 274. [[CrossRef](#)] [[PubMed](#)]
3. Zhu, S.; Zhu, C. Secure Image Encryption Algorithm Based on Hyperchaos and Dynamic DNA Coding. *Entropy* **2020**, *22*, 772. [[CrossRef](#)] [[PubMed](#)]
4. Wen, H.; Zhang, C.; Chen, P. A Quantum Chaotic Image Cryptosystem and Its Application in IoT Secure Communication. *IEEE Access* **2021**, *9*, 20481–20492. [[CrossRef](#)]
5. Gan, Z.; Chai, X.; Han, D. A Chaotic Image Encryption Algorithm Based on 3-D Bit-Plane Permutation. *Neural Comput. Appl.* **2019**, *31*, 7111–7130. [[CrossRef](#)]

6. Hua, Z.; Zhou, Y. Dynamic Parameter-Control Chaotic System. *IEEE Trans. Cybern.* **2015**, *46*, 3330–3341. [[CrossRef](#)]
7. Wen, H.; Zhang, C.; Huang, L. Security Analysis of a Color Image Encryption Algorithm Using a Fractional-Order Chaos. *Entropy* **2021**, *23*, 258. [[CrossRef](#)]
8. Khan, P.; Byun, Y. A Blockchain-Based Secure Image Encryption Scheme for the Industrial Internet of Things. *Entropy* **2020**, *22*, 175. [[CrossRef](#)]
9. Xu, L.; Li, Z.; Li, J. A Novel Bit-Level Image Encryption Algorithm Based on Chaotic Maps. *Opt. Lasers Eng.* **2016**, *78*, 17–25. [[CrossRef](#)]
10. Hua, Z.; Zhou, Y.; Bao, B. Two-Dimensional Sine Chaotification System with Hardware Implementation. *IEEE Trans. Ind. Informatics* **2020**, *2*, 887–897. [[CrossRef](#)]
11. Zhang, Y.; Xin, J.; Li, X. Overview on Routing and Resource Allocation Based Machine Learning in Optical Networks. *Opt. Fiber Technol.* **2020**, *60*, 102355. [[CrossRef](#)]
12. Wei, H.; Cui, M.; Zhang, C. Chaotic Key Generation and Application in OFDM-PON Using QAM Constellation Points. *Opt. Commun.* **2021**, *490*, 126911. [[CrossRef](#)]
13. Wu, J.; Shi, J.; Li, T. A Novel Image Encryption Approach Based on a Hyperchaotic System, Pixel-Level Filteringing with Variable Kernels, and DNA-Level Diffusion. *Entropy* **2020**, *22*, 5. [[CrossRef](#)]
14. Pourasad, Y.; Ranjbarzadeh, R.; Mardani, A. A New Algorithm for Digital Image Encryption Based on Chaos Theory. *Entropy* **2021**, *23*, 341. [[CrossRef](#)] [[PubMed](#)]
15. Wen, H.; Xu, J.; Liao, Y. A Security-Enhanced Image Communication Scheme Using Cellular Neural Network. *Entropy* **2021**, *23*, 1000. [[CrossRef](#)] [[PubMed](#)]
16. Wu, T.; Zhang, C.; Chen, Y. Compressive Sensing Chaotic Encryption Algorithms for OFDM-PON Data Transmission. *Opt. Express* **2021**, *29*, 3669–3684. [[CrossRef](#)] [[PubMed](#)]
17. Chai, X.; Fu, X.; Gan, Z. An Efficient Chaos-Based Image Compression and Encryption Scheme Using Block Compressive Sensing and Elementary Cellular Automata. *Neural Comput. Appl.* **2018**, *32*, 4961–4988. [[CrossRef](#)]
18. Hua, Z.; Zhou, Y. Exponential Chaotic Model for Generating Robust Chaos. *IEEE Trans. Syst. Man-Cybern.-Syst.* **2019**, *51*, 3713–3724. [[CrossRef](#)]
19. Li, C.; Lin, D.; Lu, J.; Hao, F. Cryptanalyzing an Image Encryption Algorithm Based on Autoblocking and Electrocardiography. *IEEE Multimed.* **2018**, *25*, 46–56. [[CrossRef](#)]
20. Wen, H.; Yu, S. Cryptanalysis of An Image Encryption Cryptosystem Based on Binary Bit Planes Extraction and Multiple Chaotic Maps. *Eur. Phys. J. Plus* **2019**, *134*, 337. [[CrossRef](#)]
21. Ma, Y.; Li, C.; Ou, B. Cryptanalysis of an Image Block Encryption Algorithm Based on Chaotic Maps. *J. Inf. Secur. Appl.* **2020**, *54*, 102566. [[CrossRef](#)]
22. Umoh, E.; Iloanusi, O.; Nnolim, U. Image Multi-Encryption Architecture Based on Hybrid Keystream Sequence Interspersed with Haar Discrete Wavelet Transform. *IET Image Process.* **2020**, *14*, 2081–2091. [[CrossRef](#)]
23. Wang, B.; Zhang, B.; Liu, X. An Image Encryption Approach on The Basis of a Time Delay Chaotic System. *Optik* **2021**, *225*, 165737. [[CrossRef](#)]
24. Elmanfalaty, R.; Alnajim, A.; Abou-Bakr, E. A Finite Precision Implementation of an Image Encryption Scheme Based on DNA Encoding and Binarized Chaotic Cores. *IEEE Access* **2021**, *9*, 136905–136916. [[CrossRef](#)]
25. Chen, L.; Li, C.; Li, C. Security Measurement of a Medical Image Communication Scheme based on Chaos and DNA coding. *J. Vis. Commun. Image Represent.* **2022**, *83*, 103424. [[CrossRef](#)]
26. ElKamchouchi, D.; Mohamed, H.; Moussa, K. A Bijective Image Encryption System Based on Hybrid Chaotic Map Diffusion and DNA Confusion. *Entropy* **2020**, *22*, 180. [[CrossRef](#)]
27. Zhang, C.; Yan, Y.; Wu, T. Phase Masking and Time-Frequency Chaotic Encryption for OFDM-PON. *IEEE Photonics J.* **2018**, *10*, 1–9. [[CrossRef](#)]
28. Zhang, C.; Zhang, W.; Chen, C. Physical-Enhanced Secure Strategy for OFDMA-PON Using Chaos and Deoxyribonucleic Acid Encoding. *J. Light. Technol.* **2018**, *36*, 1706–1712. [[CrossRef](#)]
29. Li, T.; Shi, J.; Li, X. Image Encryption Based on Pixel-Level Diffusion with Dynamic Filtering and DNA-Level Permutation with 3D Latin Cubes. *Entropy* **2019**, *21*, 319. [[CrossRef](#)]
30. Tresor, L.; Sumbwanyambe, M. A Selective Image Encryption Scheme Based on 2D DWT, Henon Map and 4D Qi Hyper-Chaos. *IEEE Access* **2019**, *7*, 103463–103472. [[CrossRef](#)]
31. Chai, X.; Zheng, X.; Gan, Z. Exploiting Plaintext-Related Mechanism for Secure Color Image Encryption. *Neural Comput. Appl.* **2019**, *32*, 8065–8088. [[CrossRef](#)]
32. Zhang, W.; Zhang, C.; Chen, C. Experimental Demonstration of Security-Enhanced OFDMA-PON Using Chaotic Constellation Transformation and Pilot-Aided Secure Key Agreement. *J. Light. Technol.* **2017**, *35*, 1524–1530. [[CrossRef](#)]
33. Wen, H.; Yu, S.; Lu, J. Breaking an Image Encryption Algorithm Based on DNA Encoding and Spatiotemporal Chaos. *Entropy* **2019**, *21*, 246. [[CrossRef](#)] [[PubMed](#)]
34. Ramasamy, P.; Ranganathan, V.; Kadry, S. An Image Encryption Scheme Based on Block Scrambling, Modified Zigzag Transformation and Key Generation Using Enhanced Logistic-Tent Map. *Entropy* **2019**, *21*, 656. [[CrossRef](#)]
35. Wu, T.; Zhang, C.; Huang, H. Security Improvement for OFDM-PON Via DNA Extension Code and Chaotic Systems. *IEEE Access* **2020**, *8*, 75119–75126. [[CrossRef](#)]

36. Hua, Z.; Zhou, Y. Image Encryption Using 2D Logistic-Adjusted-Sine Map. *Inf. Sci.* **2016**, *339*, 237–253. [[CrossRef](#)]
37. Wen, H.; Liu, Z.; Lai, H. Secure DNA-Coding Image Optical Communication Using Non-Degenerate Hyperchaos and Dynamic Secret-Key. *Mathematics* **2022**, *10*, 3180. [[CrossRef](#)]
38. Wang, K.; Gao, T.; You, D. A Secure Dual-Color Image Watermarking Scheme Based 2D DWT, SVD and Chaotic Map. *Multimed. Tools Appl.* **2022**, *81*, 6159–6190. [[CrossRef](#)]
39. Zhang, C.; Zhang, W.; He, X. Physically Secured Optical OFDM-PON by Employing Chaotic Pseudorandom RF Subcarriers. *IEEE Photonics J.* **2017**, *9*, 1–8. [[CrossRef](#)]
40. USC-SIPI Image Database. 2022. Available online: <http://sipi.usc.edu/database> (accessed on 18 September 2022).
41. Li, C.; Lin, D.; Lu, J. Cryptanalyzing an Image-Scrambling Encryption Algorithm of Pixel Bits. *IEEE Multimed.* **2017**, *24*, 64–71. [[CrossRef](#)]
42. Murillo-Escobar, M.A.; Cruz-Hernandez, C.; Abundiz-Perez, F.; López-Gutiérrez, R.M.; Acosta Del Campo, O.R. A RGB Image Encryption Algorithm Based on Total Plain Image Characteristics and Chaos. *Signal Process.* **2015**, *109*, 119–131. [[CrossRef](#)]
43. Song, C.; Qiao, Y. A Novel Image Encryption Algorithm Based on DNA Encoding and Spatiotemporal Chaos. *Entropy* **2015**, *17*, 6954–6968. [[CrossRef](#)]
44. Liang, X.; Zhang, C.; Luo, Y. Secure Key Distribution and Synchronization Method in an OFDM-PON Based on Chaos. *Opt. Express* **2022**, *30*, 18310–18319. [[CrossRef](#)]
45. Li, H.; Hua, Z.; Bao, H. Two-Dimensional Memristive Hyperchaotic Maps and Application in Secure Communication. *IEEE Trans. Ind. Electron.* **2020**, *68*, 9931–9940. [[CrossRef](#)]
46. Askar, S.; Karawia, A.; Al-Khedhairi, A. An Algorithm of Image Encryption Using Logistic and Two-Dimensional Chaotic Economic Maps. *Entropy* **2019**, *21*, 44. [[CrossRef](#)] [[PubMed](#)]
47. Arslan, A.S.; Shahid, J. Novel Image Encryption Cryptosystem Based on Binary Bit Planes Extraction and Multiple Chaotic Maps. *Eur. Phys. J. Plus* **2018**, *133*, 331. [[CrossRef](#)]
48. Yin, Q.; Wang, C. A New Chaotic Image Encryption Scheme Using Breadth-First Search and Dynamic Diffusion. *Int. J. Bifurc. Chaos Appl. Sci. Eng.* **2018**, *28*, 1850047. [[CrossRef](#)]
49. Luo, Y.; Zhang, C.; Liang, X. Secure OFDM-PON Using Three-Dimensional Selective Probabilistic Shaping and Chaos. *Opt. Express* **2022**, *30*, 25339–25355. [[CrossRef](#)]
50. Wen, H.; Ma, L.; Liu, L. High-quality Restoration Image Encryption Using DCT Frequency-domain Compression Coding and Chaos. *Sci. Rep.* **2022**, *12*, 15721–15741.